Voltage Bias Stress Effects in Metal Halide Perovskites are Strongly Dependent on Morphology and Ion Migration Pathways

ARTICLE

Voltage Bias Stress Effects in Metal Halide Perovskites are Strongly Dependent on Morphology and Ion Migration Pathways

Laura Flannery, [a] Jonathan Ogle, [a] Daniel Powel,[a] Christopher Tassone,[b] and Luisa Whittaker-Brooks*[a]

The solar-to-power power conversion efficiencies (PCEs) of metal halide perovskites (MHP) have improved over the last decade using a wide variety of methods, including composition manipulation, dopant introduction, and interfacial buffers. These methods, however, have taken little regard for the electronic and interfacial effects such alterations may cause within devices under voltage bias stress -a condition required for most device operation. We investigate how halide and cation substitution in MHP structures [specifically, $CH_3NH_3PbI_{2.87}Cl_{0.13}$ and $Cs_{0.1}(MA_{0.17}FA_{0.83})_{0.9}Pb(I_{0.83}Br_{0.17})_3$] effects the current behavior of devices while under a range of voltage bias stress in both light and dark conditions. Conducting in depth investigations into the electronic and morphological differences between these two MHP devices, we confirmed their unique voltage bias stress effects are due to intrinsic behavior within the perovskite structure. Importantly, we also determined how crystallite orientation can influence ion migration and therefore alter charge transport and current stability in MHP photovoltaic devices.

Introduction

Metal halide perovskites (MHP) have received an impressive amount of attention across many fields of research due to their tailorable semiconducting properties that create versatile functionality for a variety of optoelectronic applications such as solar cells,[1] light emitting diodes,[2] photodetectors,[3] resistive memory devices,[4] transistors,[5] and lasing devices.[6] However, regardless of the application, a common theme among the research on MHP materials besides the ability to out-perform conventional silicon-based devices, is their lack of stability.[7, 8] MHPs in ambient air when exposed to external environmental factors such as moisture, light, and/or thermal stress will degrade into their precursor materials.[9-11] When these degradation products form, they irreversibly hinder or destroy the MHP functionality which deleteriously impacts device performance. The limited durability and performance losses that result in MHP devices are why the perovskite field has been highly focused on determining how degradation in the material is occurring and methods to prevent it.[12-14]

For example, over recent years with the explosive interest in MHPs, several solutions have been proposed to improve their stability. Some of the methods that have been proven successful include cross-linking additives, encapsulation with water-proof fluorinated polymers or more simple compositional engineering of the perovskites themselves with

cation cascade techniques or partial halide ion substitution.[9, 12, 15-17] The issue remains however, that even with a resolution that prevents MHP degradation to external factors, these materials are still prone to experience internal current and voltage instabilities while under operation. Therefore, an important aspect that needs to be more carefully analyzed is the secondary effects that these instabilities may cause to device performance. As slight compositional manipulations are commonly made to MHPs to improve their performances, it becomes even more difficult to track trends observed in these materials and, therefore, easy to draw bombastic conclusions. For example, when focusing on MHP solar cell devices, it is often challenging to understand the effects that variations in current and voltage under operating conditions have on the internal mechanisms occurring in the active layer, let alone their interactions with the corresponding charge transport materials. This is supported by the significant discrepancies observed on the recorded power conversion efficiencies (PCEs) of MHP solar cell devices that only have slight differences in composition.[7, 18, 19] These differences in PCEs are not mechanistically well understood and still require much investigation.

This leads us to consider how the two primary factors that are required for MHP solar cell operation, illumination and a voltage bias, influence the intrinsic optoelectronic properties of the active layer. When a voltage bias is held across an MHP device, the resulting measured current should ideally remain constant over the time that the bias is applied. This, however, is commonly not the case and instead what is observed are bias stress effects.[20-24] Current and voltage instabilities in MHP devices are bias stress effects that contribute to the inconsistencies found in PCEs and the observed durability of the devices.

Here we investigate the bias stress effects in two types of MHP devices to elucidate the origin of the resulting current and voltage instabilities and determine material characteristics that are influential in the variation of the observed stress effects. The two MHPs utilized are a triple cation perovskite, $Cs_{0.1}(MA_{0.17}FA_{0.83})_{0.9}Pb(I_{0.83}Br_{0.17})_3$ and a mixed halide perovskite, $CH_3NH_3PbI_{2.87}Cl_{0.13}$.[7, 25] The compositional alterations of these MHPs have improved photovoltaic performance and stability when exposed to external factors (light and humidity) that would otherwise degrade the more classic MHP structure with a single cation species, commonly methylammonium, and a single halide species, commonly iodide.[26-29] By varying the halide ion composition, it is possible to tune the bandgap of the material.[30-33] Similarly, by increasing the number and type of A-site cation species, for example with the incorporation of formamidinium (FA^+), the bandgap may be adjusted to achieve a broader light absorption window.[34-36] The triple cation MHP with cesium (Cs^+) as the small third cation specie $[Cs_{0.1}(MA_{0.17}FA_{0.83})_{0.9}Pb(I_{0.83}Br_{0.17})_3]$ exhibit the highest certified efficiency (25.2%)[34, 37] due to it having a more stable crystal structure.[34] The quick crystallization of both MHP compositions $[CH_3NH_3PbI_{2.87}Cl_{0.13}$ and $Cs_{0.1}(MA_{0.17}FA_{0.83})_{0.9}Pb(I_{0.83}Br_{0.17})_3]$ does, however, allow for the formation of grain boundaries and defects.[38] Yet, MHPs have a high defect tolerance and therefore, can still perform effectively.[31, 39] Inevitably, ion vacancies also form during crystallization throughout the material, allowing for ion migration which has been shown to impact the internal device stability when under operating conditions.[34, 39-42] A common effect due to ion migration often observed in MHPs is hysteresis in the current-voltage (J-V) characteristics.[23] Hysteresis is a type of bias behavior but all bias stress effects are not exclusively hysteresis-driven. The manifestation of hysteresis in MHP devices is observed as a discrepancy in the current-voltage curve between two sweeping directions. Overcoming hysteretic effects in these devices is another primary issue that impedes the commercialization of these materials. Therefore, much work in the field of MHPs has also focused on alleviating and understanding the hysteresis observed in these materials.[1, 43-45] A successful example of this alleviation is through the addition of molecules, such as phenyl-C61-butyric acid methyl ester (PCBM), into the bulk material or as a passivation layer.[43, 46] However, the triple cation MHP, without additional passivation layers or additives has exhibited less hysteresis when compared to other MHP compositions and the reason why this hysteretic effect is lessened is in part revealed in our work while investigating the bias stress effects in these materials.[25, 47, 48]

Beyond hysteresis, another unique bias dependent phenomenon has been observed in MHP devices. A study reported on the mixed halide MHP ($CH_3NH_3PbI_{2.87}Cl_{0.13}$) exhibited a bias stress effect dependent on the initial positive voltage of the J-V sweep measurements.[22] The study provided insights into the intrinsic behavior of the mixed halide MHP and how the performance of the device can be erroneously enhanced by increasing the initial bias of the J-V sweep.[22] We investigated this bias dependent effect in triple cation MHP devices $[Cs_{0.1}(MA_{0.17}FA_{0.83})_{0.9}Pb(I_{0.83}Br_{0.17})_3]$ to understand how

this may differ in devices that display less hysteretic effects. In doing this, we can determine the underlying material properties that influence or allow for current instabilities to occur under bias stress and operating conditions. Furthermore, we believe any observed bias stress effect in our devices is attributed to the trapping of carriers into localized electronic states due to a voltage-induced bias. These trap states may be located in the active layer, at the active layer/transport layer interface, or in the transport layer/electrode interface. The longer the voltage bias is applied, the more carriers are trapped causing a spike in the observed current over time. As the voltage is released, carriers will be de-trapped and current should recover over time.

Results and discussion

In this study, we utilize a conventional n-i-p structure (n: electron transport layer, i: absorber, and p: hole transport layer) for both MHP compositions. This includes a fluorine-doped tin oxide (FTO) bottom contact, a planar titanium oxide electron transport layer (ETL), the mixed halide or triple cation MHP, a doped Spiro-O-MeTAD hole transport layer (HTL), and finally a gold top contact as displayed in **Figure 1A**. In addition to the layers that make up the device stacks, **Figure 1A** also depicts an energy level diagram to show how free charges are generated and the directional flow within the device layers. The recorded work functions of these materials are established as having good energy level alignment that allow for efficient carrier extraction and in turn high PCEs.[7] Having devices that perform efficiently and uniformly is crucial to study bias stress effects under both light and dark conditions as well as under voltages beyond the standard sweep range, between the open-circuit voltage (V_{oc}) and short circuit current (J_{sc}).

As solar cells must operate under illumination as well as under voltage bias, we investigated the voltage bias stress effects present when collecting the conventional current-voltage (J-V) responses of MHP devices under 1 sun illumination. **Figure 1B** shows the J-V curves for $CH_3NH_3PbI_{2.87}Cl_{0.13}$ mixed halide MHP photovoltaic devices as a function of voltage sweeps. As depicted, we observe a bias dependent effect resulting in a large V-shape structure that increases in intensity as the voltage sweep range increases. The large black arrow in **Figure 1B** represents the reverse sweep direction with the starting voltage of the sweep ranges varying from 0.8 V, a control voltage value below the V_{oc}, to 2.2 V, a value used as an extreme well above the V_{oc}. A starting sweep voltage of 1.2 V is considered to be the normal J-V sweep range. However, the same bias dependent effect does not occur with the sweep ranges if the sweep direction is in the opposite forward direction (**Figure S1**).[22] **Figure 1C** shows a zoomed version of the V_{oc} and J_{sc} variations as a function of voltage sweep. This allows for a better visualization of how the increase
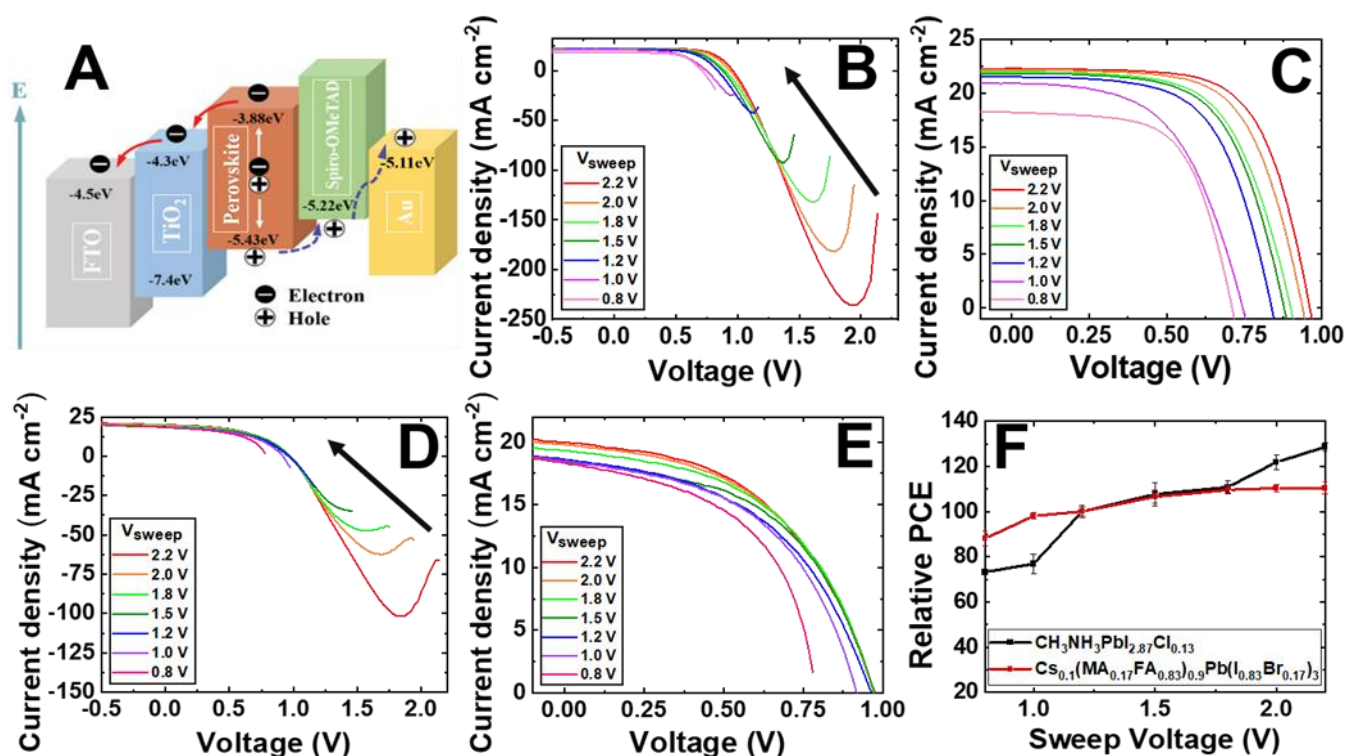
Figure 1. A) Energy diagram for a MHP photovoltaic cell. **B)** J-V curves for mixed halide MHP photovoltaic devices with increasing voltage sweep range to an extreme of 2.2 V. **C)** Zoomed-in version of the J-V plot shown in Figure 1B displaying the increase in J_{sc} and V_{oc} of the mixed halide MHP device upon increasing the voltage sweep range. **D)** J-V curves for triple cation MHP photovoltaic devices with increasing voltage sweep range to an extreme of 2.2 V. **E)** Zoomed-in version of the J-V plot presented in Figure 1D displaying the increase in J_{sc} and V_{oc} of the triple cation MHP device upon increasing the voltage sweep range. **F)** Comparison of the increases in the relative PCE for devices comprising both MHP compositions as a function of sweep voltage range. Standard error was calculated with a sample size of 20 devices for each sweep range. Device active area: 0.10 cm². Black arrows define the reverse voltage sweep direction. All J-V characteristics were acquired under visible light irradiation of 100 mWcm^{-2}.

in starting voltage not only creates this V-shape but also results in an increase in PCEs. As depicted, the V_{oc} and J_{sc} increase consistently with the increase in starting voltages and the V_{oc} specifically increases more drastically. These increases result in approximately a 30% relative increase in the PCE of $CH_3NH_3PbI_{2.87}Cl_{0.13}$ mixed halide MHP photovoltaic devices when comparing the voltage sweep starting at 2.2 V to the normal starting voltage of 1.2 V. Similarly, when examining the $[Cs_{0.1}(MA_{0.17}FA_{0.83})_{0.9}Pb(I_{0.83}Br_{0.17})_3]$ triple cation MHP photovoltaic devices, we also observe the formation of a V-shape swing at higher voltages (**Figure 1D**). However, this V-shape is significantly less steep than what is observed for the mixed halide MHP. As demonstrated in **Figure 1D**, the V-shape bias dependent effect, even when the starting voltage is increased to the extreme 2.2 V, never results in a relative PCE increase equivalent to the mixed halide MHP. In the zoomed-in version provided in **Figure 1E**, the changes in V_{oc} and J_{sc} for the triple cation MHP devices are displayed. As demonstrated, the changes in V_{oc} and J_{sc} are lessened compared to the mixed halide MHP but still show increases as the starting sweep voltage is increased. In **Figure 1F**, these differences are broken down by displaying the changes in relative PCEs observed for the mixed halide and the triple cation MHP devices as a function of the

initial sweep voltage. The PCEs for the triple cation MHP devices are increased by 10% while the PCEs for the mixed halide MHP devices are increased by over 30%.

Moreover, we find that the magnitude by which the J_{sc} increases in both triple cation and mixed halide MHP device architectures is similar implying that the overall differences in how the relative PCEs are changing are not due to the J_{sc} parameter as much as its counterpart, the V_{oc}. Low V_{oc} values are commonly the result of poor charge extraction and charge accumulation at the interface with the transport layers, which causes high interfacial recombination.[49] The improvements in V_{oc} as the starting sweep voltage bias is increased would therefore imply that less interfacial recombination is occurring. This would also mean that the interfacial recombination, especially in the mixed halide MHP devices, has a bias dependent component since the V_{oc} for the triple cation MHP devices remains relatively the same beyond the starting voltage of 1.2 V while the mixed halide devices have distinct increases in V_{oc} at every new voltage. So, the greater intensity of the V-shape voltage bias dependent effect influences the V_{oc} more directly and therefore, significantly increases the PCEs as well. For both devices, however the interfacial recombination is dependent on the sweep direction. In the forward sweep

direction, we observe the opposite effect with no V_{oc}, J_{sc} or PCE increases because the interfacial recombination would still inevitably occur when starting the sweep in the active J-V region for the photoelectric effect. Therefore, the V-shape bias dependent effect is not observed in either device when swept in the forward direction. The difference in magnitude of the bias stress effects observed for the triple cation and mixed halide MHP devices that have the same architecture outside of the perovskite active layer implies that compositional alterations are influencing primary functions involved in the device basic operation. These compositional changes alter how different biases, while under illumination, can manipulate the charge transfer and V_{oc} of the devices. Thus, we must also show if the bias stress effects in these MHP devices remain different when light is no longer involved.

To study the voltage and current bias stress effects of these MHP devices under dark conditions, we performed ON and OFF pulsed voltage experiments as a function of time. Here, we utilized the same range of voltages from 0.8 V, below the device V_{oc} to 2.2 V, largely above the V_{oc}. The pulsed voltage bias stress effects of the mixed halide MHP devices are displayed in **Figure 2A**. The different voltage biases do not seem to influence the measured current trends as they remained the same at every voltage for at least 300 seconds. Though at every voltage in **Figure 2A**, the devices consistently display a sharp current spike, when the voltage is first applied. This current spike quickly decays to a constant current until the voltage is turned OFF and back ON again. The current spike and decay are observed to occur on the order of seconds. This bias stress effect does not occur in devices containing the triple cation MHP active layer. In fact, under dark conditions, the pulsed voltage studies displayed in **Figure 2B** show no sign of bias stress effects occurring in the triple cation MHP devices. When all the different voltages are pulsed ON and OFF across the triple cation MHP devices, the current remains constant for more than 300 seconds (**Figure 2B**). This would suggest that the bias stress that is observed in the J-V curves for the triple cation MHP is exacerbated or becomes more sensitive to bias when light is involved. The same current trends for both types of MHP devices continue to be observed for at least 2600 seconds (**Figure S2**). Thus, our pulsed voltage measurements indicate that the magnitude of voltage does not influence the bias stress that is observed under dark conditions. It is also important to note that the current trends observed in our bias stress experiments are not sensitive to pulsed frequencies or the voltage bias period (**Figure S3**). There is, however, a significant difference when comparing the current trends of the mixed halide MHP devices vs. the triple cation MHP devices with the mixed halide MHP devices being the only ones that display current instabilities under voltage bias stress under dark conditions. By demonstrating the clear distinctions in the voltage bias stress effects that these two different MHPs experience, we further investigated the underlying causes of why these two compositions would cause such glaring differences in the observed bias stress effects and what MHP interactions are responsible.

Due to the MHP devices having the same n-i-p architecture, we can assume that the bias stress effects occur either as an internal or interfacial interaction that is unique to the two different MHP layers. However, to further diminish this uncertainty, bias stress experiments were also conducted on two other device architectures for both MHP compositions. These device stacks are displayed in **Figure 3A**. These include the full device stack that has been used thus far in this work, a device with no hole transport layer, and finally, one with no transport layers. The resulting current measurements of the three device stacks do not display any variance from what is observed in the original bias stress experiment. As shown in the pulsed voltage bias as a function of time, the mixed halide MHP devices result in a sharp current spike and quick decay even when all (or one) the transport layers are removed (**Figure 3B**). Simultaneously, the triple cation MHP devices still show no evidence of any bias stress effects occurring with or without transport layers (**Figure 3C**).

Due to the consistent results, when the transport layers are no longer present, we can infer that the bias stress effect is occurring as a direct result of the MHP layer itself. We believe an internal mechanism inherent to the mixed halide MHP active
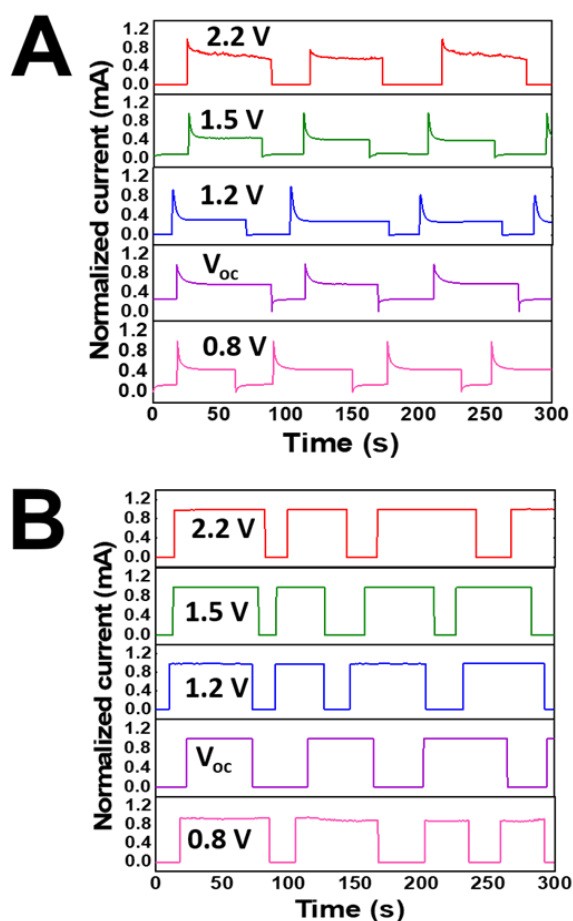

Figure 2. Bias stress experiments showing the measured current at different voltage biases between 0.8 and 2.2 V pulsed ON and OFF over time across devices comprising **A)** the mixed halide MHP and **B)** the triple cation MHP.
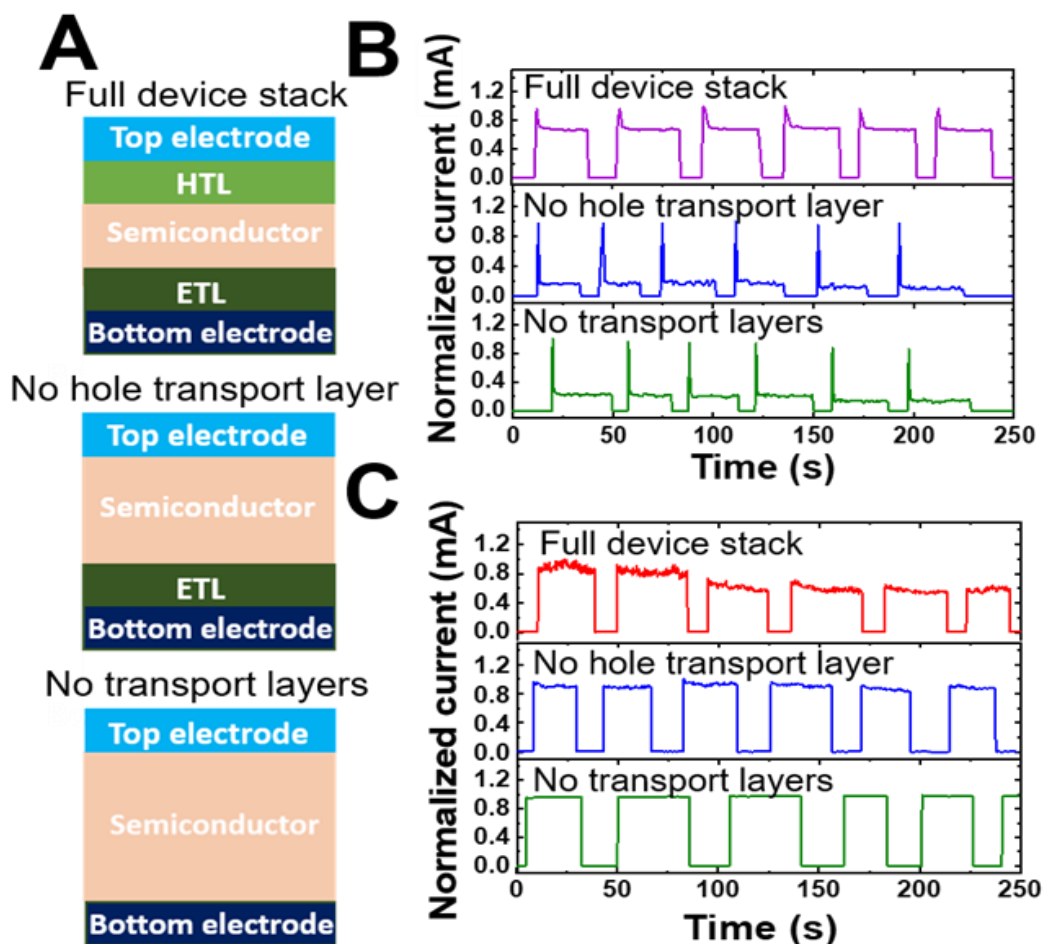
Figure 3. A) Device stack architectures with and without transport layers. Bias stress experiments for **B)** mixed halide and **C)** triple cation MHP devices, respectively. All bias stress experiments shown here were perform at a pulsed voltage bias of 0.8 V.

layer causes the current instabilities when the devices are under bias stress. Since we could determine that the bias stress is conditional to the MHP layer, the underlying structural and morphological differences of the two MHP compositions studies may uncover the reason for the observed disparities in the bias stress effects. It is well documented that the common degradation products (lead iodide, PbI_2 and methylammonium iodide, CH_3NH_3I) in MHPs are crystalline.[50, 51] Thus, by performing X-ray diffraction (XRD) studies, we can assure that the current instabilities observed are not an indication of accelerated degradation of the MHP material while under voltage bias stress. By comparing the XRD spectra for the MHP active layer of each device, before and after applying a voltage bias, we can confirm whether structural degradation and/-or atmospheric oxidation occurred during the period of analysis. **Figure 4** illustrates the XRD spectra for devices containing the mixed halide and triple cation MHP active layers before and after voltage bias stress. The green arrow at 12.6° indicates where the crystallographic reflections associated with the (001) plane for PbI_2 would appear if the bias stress or external factors such as oxidation or moisture had caused degradation of the MHP layer.[1, 47] As shown, we do not observe the formation of any degradation products due to voltage bias stress. Moreover,

the diffraction peaks at approximately 14.0° and 28.0 in **Figure 4A and 4B** displays the crystallographic reflections associated with the (110) and (220) Miller planes for both the mixed halide and the triple cation MPHs. Both crystallographic reflections do not display any significant shifting or broadening after voltage bias. The additional crystallographic reflections at higher angles depicted in **Figure 4B** are typical for the triple cation $[Cs_{0.1}(MA_{0.17}FA_{0.83})_{0.9}Pb(I_{0.83}Br_{0.17})_3]$ MHP. The influence of the smaller cesium cations with the MA^+ and FA^+ combination leads to a lower effective cation radius and, therefore a shift in the tolerance factor. This shift in tolerance factor is towards a cubic lattice structure and the additional diffraction peaks at 20.0° and 24.5° display the (112) and (211) crystallographic reflections, respectively.[47, 52-55] The peak at approximately 27.0°, however, corresponds to reflections associated with FTO and can be observed in all the XRD patterns.[56, 57] Given that these crystallite reflections remain unaltered before and after bias, the differences in bias stress effects in these MHP materials are likely innate to the physical characteristics of the crystallites themselves. Thus, it is appropriate to investigate how these two MHP compositions form and orient when cast into thin films.
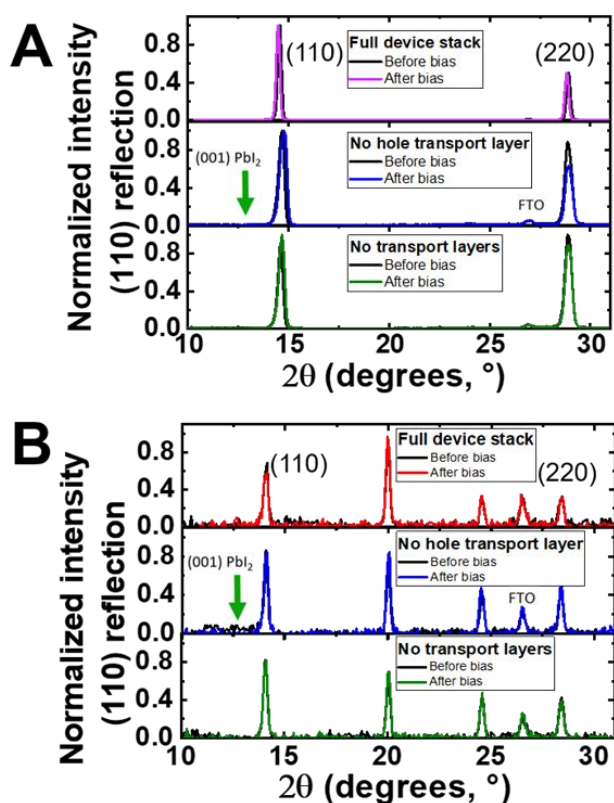
Figure 4. XRD of the three device architectures for the **A)** mixed halide MHP and **B)** triple cation MHP with the primary reflections labeled. Green arrows show where the primary PbI_2 degradation reflection peak would form in these perovskites.

Atomic force microscopy (AFM) was used to investigate the surface morphology of the mixed halide and triple cation MPHs (**Figure S4**). Both MHP compositions form relatively smooth continuous thin films with no evidence of detrimental pinholes or defects. **Figure S4A** and **S4B** shows the AFM image of a mixed halide and a triple cation MHP thin film deposited on glass. The domain sizes are larger in the mixed halide MHPs and the average surface roughness (R_q) values are also larger. Domain sizes within the mixed halide MHP film have a R_q value of 47.1 nm while the R_q values for the triple cation MHP domain sizes are 27.0 nm. The difference in domain sizes may play a role in the observed bias stress effect given that different domain sizes affect how charges can move through the MHP structure and the surface interactions with neighboring layers.[58] Domain sizes within MHPs have also previously been reported to relate to the degree of hysteresis in the material. The J-V hysteresis was found to be alleviated with larger domain sizes.[45] Since the mixed halide MHP films have larger domain sizes when compared to the triple cation MHP films and still show a higher degree of hysteresis (**Figure S5)** this would indicate that there is more at play than just the crystallize sizes influencing the hysteresis levels and bias stress effects observed in these materials. We therefore investigated further into the determination of the morphology of these MHP layers and how

crystallite orientation may influence the bias stress effects. The morphology and structure of both the mixed halide and triple cation MHP thin films were investigated via grazing incidence wide-angle X-ray scattering (GIWAXS) studies. **Figure 5** shows indexed GIWAXS images of both MHP compositions on glass substrates as well as the corresponding azimuthal line cuts of the (110) reflections. Here, the GIWAXS profiles display the formation of a crystalline mixed halide and triple cation perovskite layer. GIWAXS scattering peak assignments corroborate the formation of a tetragonal $CH_3NH_3PbI_{2.87}Cl_{0.13}$ structure with its most intense scattering peaks corresponding to reflections associated with the (110) and (220) crystallographic planes at $q = 1.04$ A^{-1} and $q = 2.08$ A^{-1}, respectively.[1, 54, 59] GIWAXS reflections for the $Cs_{0.1}(MA_{0.17}FA_{0.83})_{0.9}Pb(I_{0.83}Br_{0.17})_3$ structure corroborate the formation of a cubic structure with its most intense scattering peaks also corresponding to reflections associated with the (110) and (220) crystallographic planes at $q = 1.04$ A^{-1} and $q = 2.08$ A^{-1}, respectively.[48]

The GIWAXS patterns in **Figures 5A and 5B** demonstrate anisotropic intensities around the (110) family of planes. In particular, the (110) reflection of the mixed halide MHP in **Figure 5A** is most intense along the q_z ($q_{xy} = 0$), an indication that the (hk0) planes are preferentially oriented parallel to the substrate. Contrasting this, the GIWAXS pattern for the triple cation MHP thin films depicted in **Figure 5B** displays the intensity of the (110) reflection being stronger at 45° offset from the q_z, indicating that the same (hk0) family of planes are oriented differently with respect to the mixed halide MHP thin films.

The azimuthal line cuts of the (110) reflection shown in **Figure 5C** highlights the differences in crystallite orientation for mixed halide and triple cation MHP thin films. The black curve representing the (110) reflection for the crystallites in the mixed halide MHP thin film displays a narrow distribution when compared to the broad distribution shown in the red curve corresponding to the crystallites in the triple cation MHP thin film. In order to understand the differences in these orientational distributions, a mosaicity factor (MF) was calculated for each of these respective line cuts.[1] This allowed us to directly compare the orientational distribution of the individual components of the (110) azimuthal line cuts respective to their orientational maxima. The MF can be calculated using the following equation:

$$MF_{(hkl);\varphi_s}(\varphi) = \sum A_w(\varphi) S_{\varphi_s}(\varphi) \qquad (1)$$

This equation comprises the two sub-equations $A_w(\varphi) = \frac{A(\varphi)}{\sum A}$ and $S_{\varphi_s}(\varphi) = \frac{45 - |\varphi_s - \varphi|}{45}$. Where A_w is the weighted amplitude, the amplitude at each respective angle of the line cut divided by the sum of all amplitude values. S_ϕ is a linear transform to weigh values relative to the angle of interest, ϕ_s. MF allows for the orientation of a crystallite within a thin film to be compared on a linear scale of 1 to -1, where 1 represents perfectly parallel oriented crystallites, -1 is perfectly perpendicularly oriented crystallites, and 0 represents no orientation. This provides a

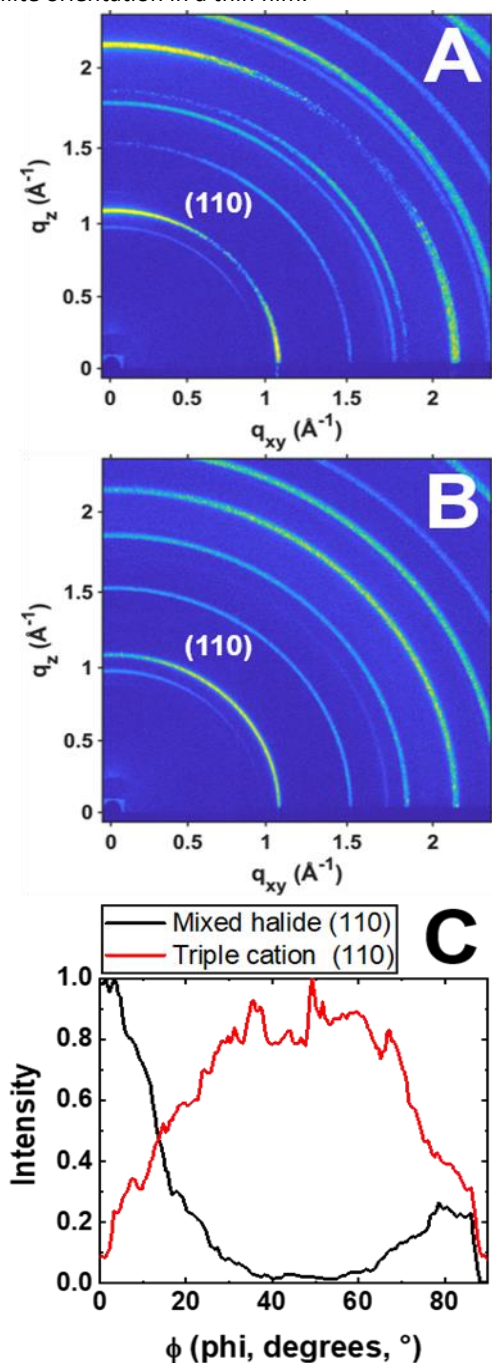comparative scale to be used to compare differences in crystallite orientation in a thin film.[1]

Figure 5. GIWAXS for the **A)** mixed halide MHP **B)** and triple cation MHP with labeled Miller indices crystallographic planes. **C)** Azimuthal linecuts of the (110) crystallographic plane for both MHP.

The mixed (110) reflection of the mixed halide MHP in **Figure 5C** shown in black presents two major orientations each along the q_z and q_{xy}. The MF for the mixed halide MHP was calculated for the (110) reflection's signal intensity centered at $\phi = 0°$ to be $MF_{(110);\ 0°} = 0.77$ which consist of 77% of the total reflection signal. The signal centered at $\phi = 90°$ was calculated to be $MF_{(110);\ 90°} = 0.67$ and contribute 23% of the (110) reflection signal. The (110) reflection of the triple cation MHP in

Figure 5C displayed in red shows a single dominant orientation along $\phi = 45°$. The MF for the triple cation MHP was calculated along the signal maxima at $\phi = 45°$ and yields a $MF_{(110);\ 45°} = 0.61$ consisting of 100% of the signal. This shows that the signal distribution along $\phi = 0°$ for the mixed halide MHP thin film displays the tightest distribution, while the signal along $\phi = 90°$ has the second tightest distribution while we observe a broad distribution of intensity for the triple cation MHP. The signal distribution does not seem to affect the bias stress effects observed since the broadest distribution is from the triple cation MHP, which displays the least amount of bias stress effects under light and dark conditions. The significant difference between these two MHPs is that the (110) crystallographic reflections are oriented 45° apart from one another. The different crystallite orientations associated with the (110) reflection in the mixed halide and triple cation MHPs can be related to the observed voltage bias stress characteristics. In MHPs, the electronic characteristics are made up of both electronic and ionic charge transport mechanisms. Furthermore, ion migration has been established as a common phenomenon that occurs in MHPs under electrical bias and illumination.[60] The extent to which ion migration becomes a limiting mechanism in MHP devices is not entirely understood, though it is known to be a cause of current-voltage sweep hysteresis.[23, 40, 61-63] Different levels of hysteresis are observed for both mixed halide and triple cation MHP devices as shown in **Figure S4**. Though the mixed halide MHP devices consistently display a more significant hysteretic effect. When an MHP device exhibits more hysteresis, it means that the resulting PCEs of the forward sweep vs. the reverse sweep differ at a greater magnitude. Since hysteresis is strongly linked to ion migration, we can assume that there is some level of ionic contributions in both kinds of MHP devices and that a higher level of ion migration is occurring in the mixed halide MHP.[40, 53] The ion migration that occurs in MHP materials is vacancy mediated.[40] MHPs are predicted to have high vacancy concentrations on the order of $10^{17}-10^{20}$ cm^{-3} even when assuming thermal equilibrium and noninteracting defects.[16, 64] The vacancy mediated diffusion of ions through the conventional hopping mechanism between neighboring positions along the anion octahedral edge has been determined for oxide and inorganic halide MHPs.[40, 64-66] As illustrated in **Figure 6A**, the Pb^{2+} ions would migrate diagonally across the cubic unit cell, or more specifically in the (110) direction.[40] The halide ion (X$^-$) migration along the octahedron edge follows the same direction along the (110) reflection plane. The cation species however, transport to a neighboring vacant A-site cage along the (100) reflection. In addition to knowing the direction in which these ion species can move with a combination of computational and experimental work, the halide ions are also known to be the most mobile ionic species within the MHP crystal lattice. Consistently in the literature, the halide ions have been reported to have the lowest activation energies (ca. 0.58 eV) and therefore can migrate with more ease.[67] The cations in MHPs have also been reported as mobile ionic species but with a higher activation energy of 0.84 eV as it involves migration through the unit cell face comprising four iodine ions as displayed in **Figure 6A**.[40, 68, 69] The Pb^{2+} ions unlike the other two ionic species have been

reported to have a high activation energy barrier of 2.31 eV, therefore suggesting a less mobile Pb sublattice.[40]

to polaron formation might alter the activation energy. As a caveat, illumination might increase the defect density thus
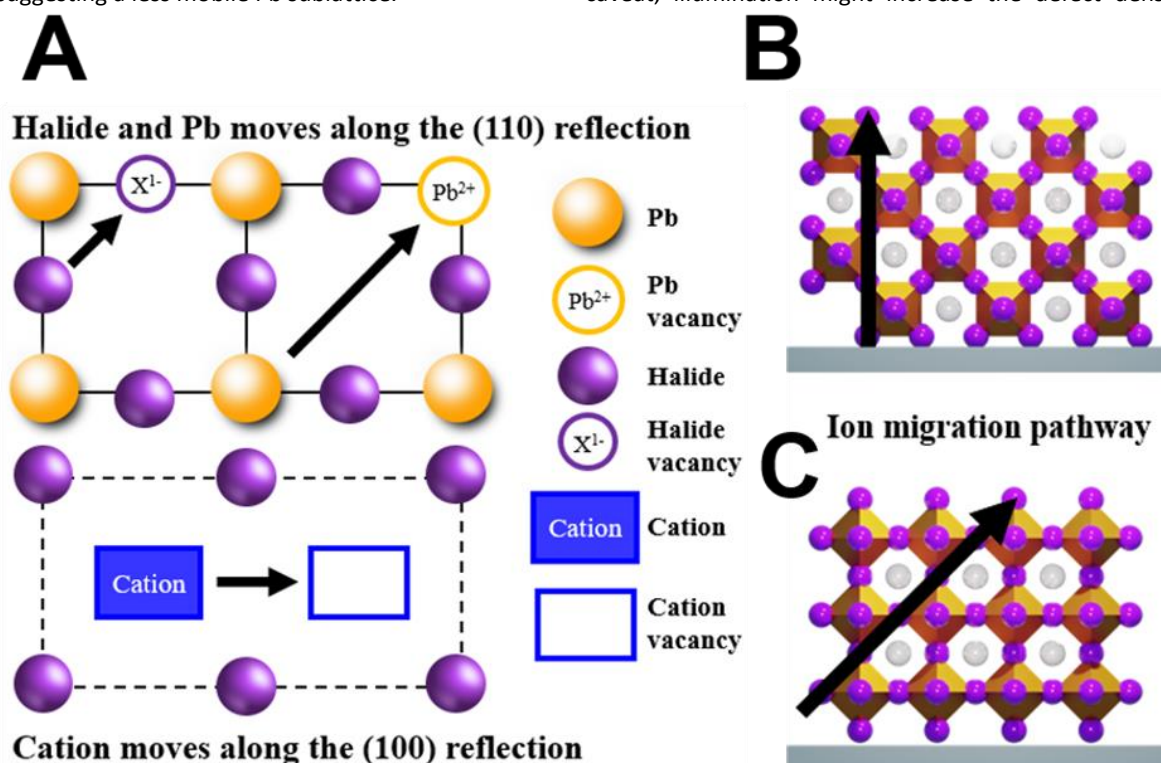

Figure 6. A) Cartoon depiction of the MHP structure displaying how the ions are understood to move along the (110) reflection or (100) reflection. **B)** Mixed halide MHP and **C)** triple cation MHP orientation relative to the substrate displaying the favorable migration pathway of the halide ions. Blue arrows represent the proposed ion migration direction based on the crystallite orientation with respect to the substrate.

Knowing the directional path in which the mobile ions travel along within the MHP lattice, we can now relate ion migration to the crystallite orientation of the mixed halide and the triple cation MHPs. **Figures 6B and 6C** depict how the mixed halide and triple cation MHP lattice structures would orient relative to the substrate when considering the independent (110) orientations as per our GIWAXS studies, respectively. The understanding of how these MHP materials orient also informs us of what ionic contributions are favorable. The blue arrows display how the halide ions would migrate through the MHP layers along their respective (110) crystallographic planes. The schematic depiction for the mixed halide MHP in **Figure 6B** has a more direct path for halide ions migration since the (110) reflection plane is perpendicular to the electrodes. While in the triple cation MHP the migration of cations would be favored, with the (100) reflection plane perpendicular to the electrodes. Both our bias stress studies support this effect under illumination and in the dark. No bias stress effects were observed in the triple cation perovskite without illumination because the activation energy of the cations is too high. However, when under illumination, there is a decrease in the activation energy of ion migration in this MHP.[17, 52, 70] This is why we observe a bias dependent effect in the triple cation MHP at higher voltage biases while under illumination. The light provides enough energy to lower the activation energy of the cations to allow for migration to the electrodes thus inducing current instabilities. We also believe that lattice distortion due

affecting the thermodynamics of ion migration.

The bias stress effects in the mixed halide MHPs are intensified due to the favored halide migration given their lower activation energies. The orientation of the crystallites within the mixed halide MHP layer, when under bias, facilitates halide migration along the (110) crystallographic plane creating direct transport channels towards the electrodes. Here, there are two effects at play. First, when the (110) plane is parallel to the electric field, a continuous network for mesoscale ion transport is created. Second, when crystallites are oriented parallel to the electric field, the driving force (or energy coupled into the ion migration) is larger so this should occur with a higher frequency. Enabling halide migration results in the current instabilities that are observed when a bias is first applied across the devices under both dark and light conditions as there is a large spike in ionic charge contributions. These bias effects are either not observed or less pronounced in the triple cation MHP. This is because the crystallite orientation observed for this MHP would favor cation migration which has a larger activation energy and therefore, we would not expect the same level of ion migration. This orientational influence would also contribute to why the triple cation MHPs have been shown to have reduced hysteretic effects when their devices are exposed to current-voltage sweeps.

Conclusions

In summary, we demonstrate that bias stress effects in MHP photovoltaic devices are influenced by variations in morphology and crystallite orientation intrinsic to the thin film. The compositional differences of the MHP active layers result in two different crystallite orientations with respect to the substrate with the triple cation MHP thin films having the most favorable orientation to constrain current instabilities under voltage bias. Thus, determining the morphology, structure, and orientation of a MHP thin film aids in a better understanding of the optoelectronic properties that arise under bias and create potential ways towards preventing the limiting effects that ion migration may have on the current stability of MHP photovoltaic devices. The broader impact of these results on the MHP field is that now depending on the desired device functionality, whether it is solar cells, transistors, LEDs, or memristors, a particular orientation can be utilized to either inhibit or promote ion migration occurring in MHP thin films. In the context of solar cell and LED devices that incorporate MHP active layers, our results indicate that it would be beneficial to have the (110) reflection plane oriented 45 degrees from the azimuth. Then, on the contrary, when MHP active layers are incorporated into memristor or transistor devices, the goal would then be to have the (110) reflection plane oriented along the azimuth as this orientation favors halide ion migration. We hope our findings lead to more work focused on engineering the orientation of MHP thin films.

Experimental

Bias Stress Dependant Studies

All device measurements, including J-V characteristics under dark and light conditions and bias stress experiments were conducted in air. J-V characteristics were taken on a Solar Cell Quantum Efficiency Measurement System (PV measurements, model QEXL). J-V characteristics under illumination were taken under AM 1.5G 100 mW/cm^2 illumination. J-V characteristics were measured by running a reverse scan (1.2 to −0.6 V) followed by a forward scan (−0.6 to 1.2 V) at a scan rate of 0.37 V/s in order to observe hysteretic effects in the devices. To investigate any bias dependent effect, the voltage sweep range was increased to an extreme of 2.2 V (2.2 V to -0.6 V). The voltage bias stress experiments conducted under dark conditions were acquired with a Keithley 2636B Source Meter on a single channel, with two points of contact on the devices. At the contact points, the voltage bias was pulsed on and off, and the current was measured over time. The voltage ranged from 0.5 V up to 2.2 V. Pulsed bias stress effect experiments were performed over 60 minutes to monitor any overall current degradation of the devices.

Characterization

A Bruker D8 diffractometer with Cu Kα radiation (λ = 1.5418 Å) was used to determine the crystal structure and phase purity of the MHP layers in devices before and after bias. The operating voltage and current were kept at 40 kV and 40 mA, respectively. The morphology and crystallite orientation of the MHP thin films were characterized via grazing incidence wide angle X-ray scattering (GIWAXS) studies. These GIWAXS experiments were conducted at the Stanford Synchrotron Radiation Lab. (SSRL, beamline 11-3). The X-ray beam energy was kept at a constant 12.7 keV with the beam aligned at a grazing angle of 0.18° with respect to the substrate. The scattered intensity was collected with a two-dimensional CCD detector comprising 3072 × 3072 pixels with a size of 73.2 μm. Sample-to-detector distance was 315 mm. All GIWAXS images were background subtracted, and polarization and absorption corrections were applied, though these corrections were generally small. Additionally, GIXSGUI was used as the graphical user interface to visualize and process GIWAXS data.[71] GIXSGUI was further used to extract 1-D line cuts along azimuthal planes for specific q spacings in order to study the overall crystallite orientation distribution and quantify the mosaicity factor for comparison.[1] Domain sizes and roughness for the MHP thin films were characterized using a Bruker Dimension Icon atomic force microscope (AFM) operated in the automated scan assist.

Solar Cell Fabrication

Patterned fluorine doped tin oxide (FTO)-coated glass substrates were cleaned in sequentially sonicated baths of Hellmanex® solution, water, acetone, and isopropyl alcohol. Following sonication, substrates were oxygen plasma cleaned for 15 min. The planar titanium oxide (TiO$_2$) electron transport layer (ETL) was deposited via RF magnetron sputtering deposition using a Denton Discovery 18 sputter system. The sputtering target was a 2 in. TiO$_2$ disc that is 0.125 in. thick, and it was used as received from the Kurt J. Lesker Company (target purity 99.99%). These sputtered films were deposited at room temperature at an applied power of 150 W under a flow of argon at a rate of 2.5 nm/min and a pressure of 4.2 mTorr. No additional gases (i.e., reactive oxygen gas) were introduced in the sputtering chamber during deposition. The sputtered TiO$_2$ film thicknesses of 35 nm were controlled by adjusting the sputtering time and deposition rate. The sample thicknesses were monitored using a profilometer. Before solar cell fabrication, sputtered TiO$_2$ samples were annealed at 450 °C for 4 h. To avoid oxygen and moisture, the substrates were transferred to a glovebox. The mixed halide, $CH_3NH_3PbI_{2.87}Cl_{0.13}$ MHP solutions were prepared with a 3:1 ratio of CH_3NH_3I: $PbCl_2$ in a 4:1 ratio of dimethylformamide and dimethyl sulfoxide. The concentration of Pb was kept to 0.8 M. The triple cation, $Cs_{0.1}(MA_{0.17}FA_{0.83})_{0.9}Pb(I_{0.83}Br_{0.17})_3$ perovskite solutions were prepared with the individual addition of each cation and lead halide component in 1 ml of the same 4:1 ratio of dimethylformamide and dimethyl sulfoxide. MHP solutions were spun-cast atop the ETL-coated FTO glass substrate under inert atmosphere at 2000 rpm for 10 s and 6000 rpm for 30 s with a chlorobenzene antisolvent wash deposited during the last 15 s. The MHP layer formed during spin-coating was annealed at 100 °C for 2 h. Afterward, the hole transporting layer (HTL) was deposited by spin coating at 4000 rpm for 15 s.

The HTL was prepared by dissolving 72.3 mg of N2,N2,N2′,N2′,N7,N7,N7′,N7′-octakis(4-methoxyphenyl)-9,9′-spirobi[9H-fluorene]-2,2′,7,7′-tetramine (Spiro-O-MeTAD), 28.8 μL of 4-tert-butylpyridine (TBP), and 17.5 μL of a lithium bis(trifluoromethylsulfonyl)imide (Li-TFSI) solution (520 mg of LiTFSI in 1 mL of acetonitrile). This mixture was dissolved in 1 mL of chlorobenzene. To complete the solar cells, a 100-nm-thick layer of Au was deposited by thermal evaporation through stencil masks as top electrodes.

Conflicts of interest
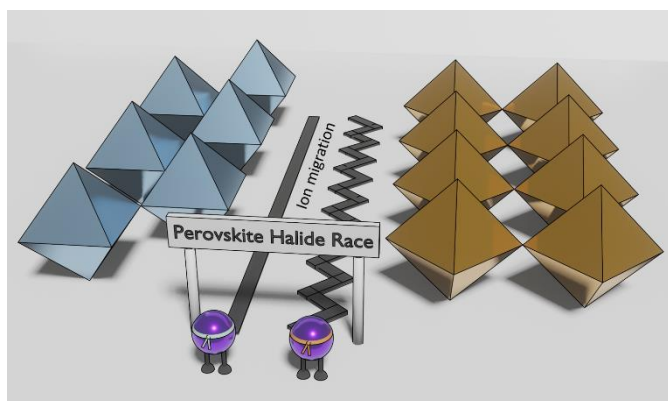
There are no conflicts to declare.

Acknowledgements

References

1.   W. J. Nimens, S. J. Lefave, L. Flannery, J. Ogle, D.-M. Smilgies, M. T. Kieber-Emmons and L. Whittaker-Brooks, *Angew. Chem. Int. Ed.*, 2019, **58**, 13912-13921.

2.   H. Cho, S.-H. Jeong, M.-H. Park, Y.-H. Kim, C. Wolf, C.-L. Lee, J. H. Heo, A. Sadhanala, N. Myoung, S. Yoo, S. H. Im, R. H. Friend and T.-W. Lee, *Science*, 2015, **350**, 1222.

3.   L. Dou, Y. Yang, J. You, Z. Hong, W.-H. Chang, G. Li and Y. Yang, *Nat. Commun.*, 2014, **5**, 5404.

4.   J. Choi, S. Park, J. Lee, K. Hong, D.-H. Kim, C. W. Moon, G. D. Park, J. Suh, J. Hwang, S. Y. Kim, H. S. Jung, N.-G. Park, S. Han, K. T. Nam and H. W. Jang, *Adv. Mater.*, 2016, **28**, 6562-6567.

5.   S. P. Senanayak, B. Yang, T. H. Thomas, N. Giesbrecht, W. Huang, E. Gann, B. Nair, K. Goedel, S. Guha, X. Moya, C. R. McNeill, P. Docampo, A. Sadhanala, R. H. Friend and H. Sirringhaus, *Sci. Adv.*, 2017, **3**, e1601935.

6.   G. Xing, N. Mathews, S. S. Lim, N. Yantara, X. Liu, D. Sabba, M. Grätzel, S. Mhaisalkar and T. C. Sum, *Nat. Mater.*, 2014, **13**, 476-480.

7.   A. K. Jena, A. Kulkarni and T. Miyasaka, *Chem. Rev.*, 2019, **119**, 3036-3103.

8.   J. Ye, H. Zheng, L. Zhu, G. Liu, X. Zhang, T. Hayat, X. Pan and S. Dai, *Solar RRL*, 2017, **1**, 1700125.

9.   Z. Ahmad, M. A. Najeeb, R. A. Shakoor, A. Alashraf, S. A. Al-Muhtaseb, A. Soliman and M. K. Nazeeruddin, *Sci. Rep.*, 2017, **7**, 15406.

10.   A. M. A. Leguy, Y. Hu, M. Campoy-Quiles, M. I. Alonso, O. J. Weber, P. Azarhoosh, M. van Schilfgaarde, M. T. Weller, T. Bein, J. Nelson, P. Docampo and P. R. F. Barnes, *Chem. Mater.*, 2015, **27**, 3397-3407.

11.   R. J. Sutton, G. E. Eperon, L. Miranda, E. S. Parrott, B. A. Kamino, J. B. Patel, M. T. Hörantner, M. B. Johnston, A. A. Haghighirad, D. T. Moore and H. J. Snaith, *Adv. Energy Mater.*, 2016, **6**, 1502458.

12.   J.-W. Lee, D.-H. Kim, H.-S. Kim, S.-W. Seo, S. M. Cho and N.-G. Park, *Adv. Energy Mater.*, 2015, **5**, 1501310.

13.   S. Seo, S. Jeong, C. Bae, N.-G. Park and H. Shin, *Adv. Mater.*, 2018, **30**, 1801010.

14.   I. C. Smith, E. T. Hoke, D. Solis-Ibarra, M. D. McGehee and H. I. Karunadasa, *Angew. Chem. Int. Ed.*, 2014, **53**, 11232-11235.

15.   S. D. Stranks, R. L. Z. Hoye, D. Di, R. H. Friend and F. Deschler, *Adv. Mater.*, 2019, **31**, 1803336.

16.   A. Walsh, D. O. Scanlon, S. Chen, X. G. Gong and S.-H. Wei, *Angew. Chem. Int. Ed.*, 2015, **54**, 1791-1794.

17.   J. Xing, Q. Wang, Q. Dong, Y. Yuan, Y. Fang and J. Huang, *Phys. Chem. Chem. Phys.*, 2016, **18**, 30484-30490.

18.   G. A. Casas, M. A. Cappelletti, A. P. Cédola, B. M. Soucase and E. L. Peltzer y Blancá, *Superlattices Microstruct.*, 2017, **107**, 136-143.

19.   X. Zheng, B. Chen, J. Dai, Y. Fang, Y. Bai, Y. Lin, H. Wei, Xiao C. Zeng and J. Huang, *Nature Energy*, 2017, **2**, 17102.

20.   B. Chen, X. Zheng, M. Yang, Y. Zhou, S. Kundu, J. Shi, K. Zhu and S. Priya, *Nano Energy*, 2015, **13**, 582-591.

21.   K. Domanski, E. A. Alharbi, A. Hagfeldt, M. Grätzel and W. Tress, *Nat. Energy*, 2018, **3**, 61-67.

22.   M. Lyu, J.-H. Yun, R. Ahmed, D. Elkington, Q. Wang, M. Zhang, H. Wang, P. Dastoor and L. Wang, *J. Colloid Interface Sci.*, 2015, **453**, 9-14.

23.   W. Tress, N. Marinova, T. Moehl, S. M. Zakeeruddin, M. K. Nazeeruddin and M. Grätzel, *Energy Environ. Sci.*, 2015, **8**, 995-1004.

24.   P. Yadav, D. Prochowicz, E. A. Alharbi, S. M. Zakeeruddin and M. Grätzel, *J. Mater. Chem. C*, 2017, **5**, 7799-7805.

25.   M. Saliba, J.-P. Correa-Baena, C. M. Wolff, M. Stolterfoht, N. Phung, S. Albrecht, D. Neher and A. Abate, *Chem. Mater.*, 2018, **30**, 4193-4201.

26.   D. Bryant, N. Aristidou, S. Pont, I. Sanchez-Molina, T. Chotchunangatchaval, S. Wheeler, J. R. Durrant and S. A. Haque, *Energy Environ. Sci.*, 2016, **9**, 1655-1660.

27.   J. A. Christians, P. A. Miranda Herrera and P. V. Kamat, *J. Am. Chem. Soc.*, 2015, **137**, 1530-1538.

28.   M.-c. Kim, N. Ahn, E. Lim, Y. U. Jin, Peter V. Pikhitsa, J. Heo, S. K. Kim, H. S. Jung and M. Choi, *J. Mater. Chem. A*, 2019, **7**, 12075-12085.

29.   D. Lan, *Prog. Photovoltaics: Res. Appl…*, 2020, **28**, 533-537.

30.   R. G. Balakrishna, S. M. Kobosko and P. V. Kamat, *ACS Energy Lett.*, 2018, **3**, 2267-2272.

31.   H. Huang, M. I. Bodnarchuk, S. V. Kershaw, M. V. Kovalenko and A. L. Rogach, *ACS Energy Letters*, 2017, **2**, 2071-2083.

32.   M. V. Kovalenko, L. Protesescu and M. I. Bodnarchuk, *Science*, 2017, **358**, 745.

33.   C. M. Sutter-Fella, Y. Li, M. Amani, J. W. Ager, F. M. Toma, E. Yablonovitch, I. D. Sharp and A. Javey, *Nano Lett.*, 2016, **16**, 800-806.

34.   C. Dong, Z.-K. Wang and L.-S. Liao, *Energy Technol.*, 2020, **8**, 1900804.

35.   C. U. Kim, J. C. Yu, E. D. Jung, I. Y. Choi, W. Park, H. Lee, I. Kim, D.-K. Lee, K. K. Hong, M. H. Song and K. J. Choi, *Nano Energy*, 2019, **60**, 213-221.

36. C. Liu, M. Hu, X. Zhou, J. Wu, L. Zhang, W. Kong, X. Li, X. Zhao, S. Dai, B. Xu and C. Cheng, *NPG Asia Mater.*, 2018, **10**, 552-561.

37. https://www.nrel.gov/pv/cell-efficiency.html, Accessed June 2020.

38. W. Ke, C. Xiao, C. Wang, B. Saparov, H.-S. Duan, D. Zhao, Z. Xiao, P. Schulz, S. P. Harvey, W. Liao, W. Meng, Y. Yu, A. J. Cimaroli, C.-S. Jiang, K. Zhu, M. Al-Jassim, G. Fang, D. B. Mitzi and Y. Yan, *Adv. Mater.*, 2016, **28**, 5214-5221.

39. H. Lee, S. Gaiaschi, P. Chapon, D. Tondelier, J.-E. Bourée, Y. Bonnassieux, V. Derycke and B. Geffroy, *J. Phys. Chem. C*, 2019, **123**, 17728-17734.

40. C. Eames, J. M. Frost, P. R. F. Barnes, B. C. O'Regan, A. Walsh and M. S. Islam, *Nat. Commun.*, 2015, **6**, 7497.

41. J.-W. Lee, S.-G. Kim, J.-M. Yang, Y. Yang and N.-G. Park, *APL Mater.*, 2019, **7**, 041111.

42. J. Yang, C. Liu, C. Cai, X. Hu, Z. Huang, X. Duan, X. Meng, Z. Yuan, L. Tan and Y. Chen, *Adv. Energy Mater.* 2019, **9**, 1900198.

43. Y. Zhong, M. Hufnagel, M. Thelakkat, C. Li and S. Huettner, *Adv. Funct. Mater.*, 2020, **30**, 1908920.

44. G. A. Sepalage, S. Meyer, A. Pascoe, A. D. Scully, F. Huang, U. Bach, Y.-B. Cheng and L. Spiccia, *Adv. Funct. Mater.*, 2015, **25**, 5650-5661.

45. H.-S. Kim and N.-G. Park, *J. Phys. Chem. Lett.*, 2014, **5**, 2927-2934.

46. D.-Y. Son, J.-W. Lee, Y. J. Choi, I.-H. Jang, S. Lee, P. J. Yoo, H. Shin, N. Ahn, M. Choi, D. Kim and N.-G. Park, *Nat. Energy*, 2016, **1**, 16081.

47. M. Saliba, T. Matsui, J.-Y. Seo, K. Domanski, J.-P. Correa-Baena, M. K. Nazeeruddin, S. M. Zakeeruddin, W. Tress, A. Abate, A. Hagfeldt and M. Grätzel, *Energy Environ. Sci.*, 2016, **9**, 1989-1997.

48. R. Singh, S. Sandhu, H. Yadav and J.-J. Lee, *ACS Appl. Mater. Interfaces*, 2019, **11**, 29941-29949.

49. U. K. Thakur, P. Kumar, S. Gusarov, A. E. Kobryn, S. Riddell, A. Goswami, K. M. Alam, S. Savela, P. Kar, T. Thundat, A. Meldrum and K. Shankar, *ACS Appl. Mater. Interfaces*, 2020, **12**, 11467-11478.

50. T. A. Berhe, W.-N. Su, C.-H. Chen, C.-J. Pan, J.-H. Cheng, H.-M. Chen, M.-C. Tsai, L.-Y. Chen, A. A. Dubale and B.-J. Hwang, *Energy Environ. Sci.*, 2016, **9**, 323-356.

51. C.-Y. Chang, Y.-C. Huang, C.-S. Tsao and W.-F. Su, *ACS Appl. Mater. Interfaces*, 2016, **8**, 26712-26721.

52. B. Murali, E. Yengel, W. Peng, Z. Chen, M. S. Alias, E. Alarousu, B. S. Ooi, V. Burlakov, A. Goriely, M. Eddaoudi, O. M. Bakr and O. F. Mohammed, *J. Phys. Chem. Lett.*, 2017, **8**, 137-143.

53. B. Murali, H. K. Kolli, J. Yin, R. Ketavath, O. M. Bakr and O. F. Mohammed, *ACS Mater. Lett.*, 2020, **2**, 184-214.

54. W. J. Nimens, J. Ogle, A. Caruso, M. Jonely, C. Simon, D. Smilgies, R. Noriega, M. Scarpulla and L. Whittaker-Brooks, *ACS Appl. Energy Mater.*, 2018, **1**, 602-615.

55. C. Yi, J. Luo, S. Meloni, A. Boziki, N. Ashari-Astani, C. Grätzel, S. M. Zakeeruddin, U. Röthlisberger and M. Grätzel, *Energy Environ. Sci.*, 2016, **9**, 656-662.

56. Z. Ren, A. Ng, Q. Shen, H. C. Gokkaya, J. Wang, L. Yang, W.-K. Yiu, G. Bai, A. B. Djurišić, W. W.-f. Leung, J. Hao, W. K. Chan and C. Surya, *Sci. Rep.*, 2014, **4**, 6752.

57. S.-H. Wu, M.-Y. Lin, S.-H. Chang, W.-C. Tu, C.-W. Chu and Y.-C. Chang, *J. Phys. Chem. C*, 2018, **122**, 236-244.

58. H. Khassaf, S. K. Yadavalli, Y. Zhou, N. P. Padture and A. I. Kingon, *J. Phys. Chem. C*, 2019, **123**, 5321-5325.

59. K. W. Tan, D. T. Moore, M. Saliba, H. Sai, L. A. Estroff, T. Hanrath, H. J. Snaith and U. Wiesner, *ACS Nano*, 2014, **8**, 4730-4739.

60. N. E. Courtier, J. M. Cave, J. M. Foster, A. B. Walker and G. Richardson, *Energy Environ. Sci.*, 2019, **12**, 396-409.

61. S. Meloni, T. Moehl, W. Tress, M. Franckevičius, M. Saliba, Y. H. Lee, P. Gao, M. K. Nazeeruddin, S. M. Zakeeruddin, U. Rothlisberger and M. Graetzel, *Nat. Commun.*, 2016, **7**, 10334.

62. S. van Reenen, M. Kemerink and H. J. Snaith, *J. Phys. Chem. Lett.*, 2015, **6**, 3808-3814.

63. T.-Y. Yang, G. Gregori, N. Pellet, M. Grätzel and J. Maier, *Angew. Chem. Int. Ed.*, 2015, **54**, 7905-7910.

64. Y. Luo, P. Khoram, S. Brittman, Z. Zhu, B. Lai, S. P. Ong, E. C. Garnett and D. P. Fenning, *Adv. Mater.*, 2017, **29**, 1703451.

65. M. Cherry, M. S. Islam and C. R. A. Catlow, *J. Solid State Chem.*, 1995, **118**, 125-132.

66. J. Mizusaki, K. Arai and K. Fueki, *Solid State Ionics*, 1983, **11**, 203-211.

67. C. Eames, J. M. Frost, P. R. Barnes, B. C. O'Regan, A. Walsh and M. S. Islam, *Nat. Commun.*, 2015, **6**, 7497.

68. A. M. A. Leguy, J. M. Frost, A. P. McMahon, V. G. Sakai, W. Kockelmann, C. Law, X. Li, F. Foglia, A. Walsh, B. C. O'Regan, J. Nelson, J. T. Cabral and P. R. F. Barnes, *Nat. Commun.*, 2015, **6**, 7124.

69. M. T. Weller, O. J. Weber, P. F. Henry, A. M. Di Pumpo and T. C. Hansen, *Chem. Commun.*, 2015, **51**, 4180-4183.

70. T. Leijtens, G. E. Eperon, S. Pathak, A. Abate, M. M. Lee and H. J. Snaith, *Nat. Commun.*, 2013, **4**, 2885.

71. Z. Jiang, *J. Appl. Crystallogr.*, 2015, **48**, 917-926.

We determined how morphology, electronic and interfacial interactions affect metal halide perovskite solar cells under voltage bias stress. We also believe our findings provide fundamental insights into the discrepancies in the power conversion efficiencies of MHP solar cells observed across many different research groups.